Raman Spectral Imaging for the Determination of Structure and Dynamics of Human Cells

M.Diem

Laboratory for Spectral Diagnosis

Department of Chemistry and Chemical Biology

Northeastern University, Boston, MA 02115 USA

Jan 26, 2009

Summary

In this contribution, the applications of a laser-based spectroscopic method to elucidate cellular structure and dynamics will be introduced. This method, based on Raman scattering, has now reached a level of sophistication that makes is competitive with more classical methods of cellular biological imaging techniques, such as confocal fluorescence microscopy, while offering the advantage of being minimally invasive (and thus, can be applied to living cells) and can be implemented without external labels.

The majority of this contribution deals with applications of classical, spontaneous Raman spectroscopy. In order to obtain microscopic images based on classical Raman spectroscopy, two major conceptual steps had to be implemented. First, Raman spectroscopy had to be coupled with microscopic methods, and a new instrumental method, Raman micro-spectroscopy (also known as Raman microscopy) was born. The second step involves the collection of spatially resolved spectroscopic data by raster-scanning the focused laser beam over the sample, or by moving the sample through the laser focus in a raster pattern *via* a high resolution microscope stage. The resulting datasets can be converted into spectral images, as discussed later.

While Raman micro-spectroscopy has been around for a couple of decades, its application to biological questions was hampered by the weak intensities of the Raman effect and the presence of a fluorescent background, which made collection of large images impractical. Within the past five years, however, instrumental advances have made it possible to collect an individual Raman spectrum from a focused, microscopic laser spot in less than 500 ms; thus, datasets of 10,000 to 20,000 individual spectra can be collected in a few hours' time. Yet, the low intensity of Raman scattering makes these datasets quite noisy, and construction of images from these datasets was, in general, unsatisfactory. Multivariate chemometric methods of analysis, however, now allow the analysis of such datasets for small, but recurring spectral features and construct spectral maps that reveal enormous biochemical detail. Some of these multivariate analysis methods were developed originally for the evaluation of remote sensing data from orbiting satellites in order to detect subsurface water or mineral deposits. Other multivariate methods were developed for the interpretation of genetic data in bacterial strains. Yet all these methods have in common that large datasets are available that have small, but correlated changes in some properties that can be extracted and analyzed.

The use of cluster analysis to construct Raman spectral images was pioneered by the research group of C.Otto in The Netherlands [1]. We extended these principles to include different statistical methods, such as Principal Component Analysis (PCA), Vertex Component Analysis (VCA) and Hierarchical Cluster Analysis (HCA) in a program toolbox for the routine analysis of Raman (and infrared) spectral datasets of individual cells and tissue sections. These methods will be introduced in some detail in this contribution, and applied to various problems in cellular biology.

In the final section, we present the background of more recent Raman technologies that have increased the data acquisition speed over hundredfold compared to the methods described in the main part of this chapter. With these new developments, Raman spectral imaging techniques are poised to become major new methods for real-time, label-free visualization of processes in cellular biology.

1. Introduction

One of the major goals in modern biological, biomedical and pharmaceutical research is the depiction of human cells and sub-cellular organization, and the dynamics of processes occurring in living cells, in three dimensions using label-free imaging methodology. The rational for these efforts is the prospect of following metabolic processes and pathways in both normal and abnormal (diseased) cells, and using this information to device new methods to treat cellular abnormality.

The last decades have seen enormous progress in the quest for imaging methods depicting cells and their components. In terms of a static understanding of cellular structure, electron microscopy has probably contributed more than any other technique for visualizing sub-cellular organization and structure. However, electron microscopy is a rather invasive procedure that does not lend itself for the determination of dynamic processes in live cells. High resolution, confocal laser-based fluorescent microscopic methods, on the other band, provide a less invasive view of cellular structure and dynamics, and has revealed a plethora of information of processes in fixed and living cells at the molecular level. The confocal nature of laser-based fluorescence microscopy allows the construction of three-dimensional images at a spatial resolution determined by the Rayleigh criterion derived for optical microscopy which limits the lateral resolution to about the wavelengths of the probing light, and the axial resolution to about twice this value (see below). Consequently, the smallest voxel that can be probed in fluorescence microscopy, utilizing blue or near-UV lasers for excitation, is about 300 nm · 300 nm · 600 nm in size. At this level of spatial resolution, the binding of labeled substrates to a receptor cannot be directly observed, although the accumulation of substrates in a localized region can just be detected. Thus, the tool of confocal fluorescence microscopy is just about sufficiently sensitive to study fundamental processes of biological and biomedical significance.

However, in order to observed fluorescence signals from most biological systems, fluorescent probes need to be attached to the target of interest. Fluorescent probes can be organic fluorophores, fluorescent biomolecules or nano-particles that are covalently or otherwise linked to the molecules to be studied. The attachment of such probes, however, may affect the mobility and binding properties, and the systems to be observed may be perturbed as compared to their native state.

We therefore have utilized imaging methodology that uses inherent spectral signatures of the molecules whose properties and dynamics are of interest, namely Raman Micro-spectral Imaging. Raman spectroscopy is a well-established laser scattering technique that monitors the vibrational spectrum of the sample. Vibrational Raman scattering can be observed microscopically using instrumentation very similar to laser fluorescence microscopy. Since Raman scattering is an extremely feeble effect, and much weaker than fluorescence emission, the instrumentation used for the observation of Raman microscopy requires highly sensitive detection and careful processing of the scattered photons. Nevertheless, the scattered Raman intensities form each voxel are contaminated by detector shot noise, which necessitates the use of sophisticated image reconstruction tools based on multivariate analysis. The methodology developed at the Laboratory for Spectral Diagnosis (LSpD) constructs pseudo-color images of cells using these analysis tools to extract biological and biomedical information contained in the Raman signals.

2. Background

As pointed out in the Introduction, Raman Micro-spectroscopy and related non-linear Raman techniques have recently been applied to image human cells and tissues at the same spatial resolution as afforded by fluorescence microscopy. However, Raman-based imaging can be carried out as a label-free method that relies on the contrast provided by the vibrational spectra of molecules. In this section, we shall explore the fundamentals of vibrational Raman spectroscopy and contrast it to the phenomena which give rise to fluorescence emission

2.1 Raman Spectroscopy

Raman spectroscopy is a form of vibrational spectroscopy that samples the same molecular vibrational states [2] as does infrared (IR) spectroscopy. However, Raman spectroscopy utilizes a scattering mechanism to excite the molecules into vibrationally excited states, whereas in IR spectroscopy, a direct, dipole-mediated transition from the vibrational ground to vibrationally excited states is observed as absorption of incident light. Scattering phenomena are much less likely to occur than absorption processes; furthermore, the scattering efficiency increases with the forth power of the frequency of the exciting light. As a consequence of these two conditions, visible laser light is commonly used for excitation, since lasers produce a large photons flux, and since the high frequency (short wavelength) of visible laser light produces large scattered intensities.

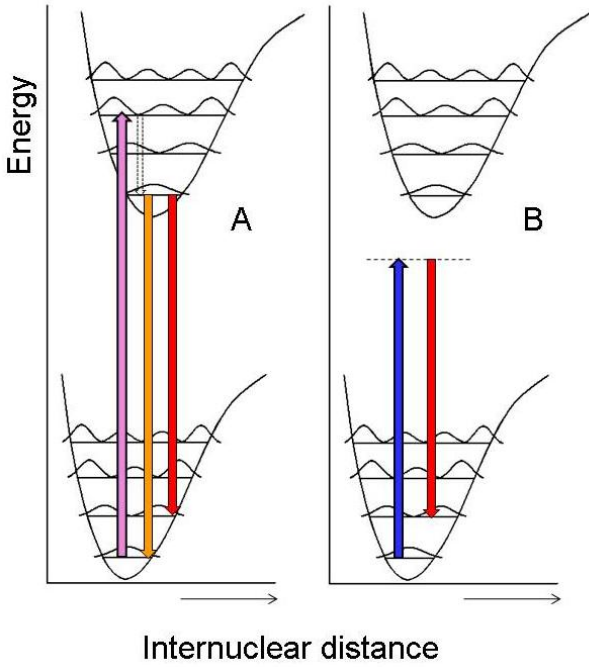

Figure 1. Comparison of excitation processes in fluorescence and Raman spectroscopy.

Raman spectroscopy resembles laser fluorescence microscopy in that monochromatic laser light is used to excite molecules as shown in Figure 1A. Here, the ground electronic state of a simple (for example, a diatomic molecule) is shown by the potential function at lower left, with the vibrational energy levels and squared wavefunctions indicated. The potential curve at the upper left represents the electronically excited state with the appropriate vibrational levels. In fluorescence, the molecules are excited into a vibrationally excited state of the electronically excited state by absorption of a photon shown as the violet up-arrow. The particular vibronic state excited depends on the Franck-Condon overlap between the vibronic ground and excited state wavefunctions.

Before re-emission of the absorbed photon can occur, the excited vibronic state may deactivate non-radiatively as shown by the dashed down-arrow in Figure 1A into the vibrational ground state of the electronically excited state. From there, photons of reduced energy (red-shifted) are emitted to the vibrationally excited states of the electronic ground state. Consequently, a fluorescence spectrum may consist of several bands spaced by the vibrational energy.

In Raman spectroscopy, shown schematically in Figure 1B, the incident laser photon, shown by the blue up-arrow, momentarily promotes the system into a “virtual” state, indi-

cated by the dashed horizontal line. As the name implies, this is not a real vibronic state; and the principle of the virtual state becomes obvious when one considers a colorless molecule interacting with a visible laser beam. The fact that the molecule is colorless indicates that there is no real energy level in the energy range of visible electromagnetic radiation. Thus, the theory of Raman scattering, developed originally in 1934 by Placzek [3], is based on the fact that the electric field of the laser creates the virtual states *via* the dielectric susceptibility (on the macroscopic level) or the molecular polarizability (on the microscopic level). This will be discussed in more detail below.

A red-shifted photon subsequently is scattered, or emitted from the virtual state, as indicated by the red down-arrow in Figure 1B, and the system returns to the vibrationally excited state of the electronic ground state. Thus, both fluorescence and Raman spectroscopy are vibronic effects; however, fluorescence probes more of the electronic states whereas Raman spectroscopy probes the vibrational states of a molecule. However, Raman scattering is at least 6 orders of magnitude weaker than fluorescence, and consequently, could not be observed microscopically in human cells until recently [4].

We now return to the discussion of the polarizability, which is responsible for permitting the interaction of a photon with a molecular system in the absence of a (dipole-allowed) direct absorption process. The Raman intensity scattered into 4π steradian is given by Eqn. 1:

$$I_s = \frac{8\pi \nu_s^4}{9c^4} I_0 \sum |(\alpha_{\rho\sigma})_{gf}|^2 \qquad (1)$$

where I_s denotes the scattered intensity for a given normal mode, ν_s is the frequency of the photons scattered by a given normal mode, and I_o is the incident intensity of the exciting radiation. All other symbols have their usual meaning.

$\alpha_{\sigma\rho}$ is the polarizability tensor derivative with respect to the normal coordinate, with the subscripts $\sigma\rho$ denoting all permutations of the Cartesian x,y and z components. The subscripts gf denote the ground and final vibrational states of the molecule, and indicate which the normal mode of the molecule is populated by the Raman process. The polarizability tensor elements can be described in terms of the previous discussion, namely that the light creates its own "virtual state", by Eqn. 2:

$$(\alpha_{\rho\sigma})_{gf} = \frac{1}{h} \sum_e \frac{\langle f|\mu_\rho|e\rangle\langle e|\mu_\sigma|g\rangle}{\nu_{eg} - \nu_0 + i\Gamma_e} + \frac{\langle f|\mu_\sigma|e\rangle\langle e|\mu_\rho|g\rangle}{\nu_{ef} + \nu_0 + i\Gamma_e} \qquad (2)$$

Here, the polarizability tensor elements are expressed as (upward) dipole transition moments between the ground state g and a real electronic state e, and the (downward) transition between the real electronic state e and the final state *f*, which is the vibrationally excited state. The product of these real dipole transition moments is weighted by the energy difference between the real electronic state energy ν_{eg} and the exciting laser frequency ν_o in the denominator. These transition moment products are summed over all electronic excited states, and it is obvious that electronic transitions very different in energy from the laser excitation contribute less to the polarizability tensor elements than transitions that fall very close to the exciting wavelength.

2.2 Experimental Methods: Raman Microspectroscopy

Raman Microspectroscopy (RMS) was first reported by Delhaye and Dhamelincourt in 1975 [5]. In RMS, the laser beam is focused into the sample using a microscope objective,

and the backscattered Raman photons are collected through the same objective. The Rayleigh scattering and back-reflected laser light are removed from the sample by a notch or bandpass filter, before the scattered photons are wavelength sorted by a monochromator and detected *via* a CCD camera. RMS became a very feasible technique with the advent of dielectrically coated filters which allow the reduction of Rayleigh scattering and reflected laser intensity by typically 8 orders of magnitude. Before these filters were readily available, double or triple monochromators were used to discriminate Raman scattering from the accompanying stray light, at the expense of low overall throughput.

Raman microspectral images reported here were acquired using a WITec, Inc. (Ulm, Germany) Model CRM 2000 Confocal Raman Microscope, which will be described in some detail next. Excitation (ca. 30 mW each at 488, 514.5 or 632.8 nm) is provided by a HeNe or an air-cooled Ar ion laser (Melles Griot, Model 05-LHP-928 and 532, respectively). Exciting laser radiation is coupled into a Zeiss microscope through a wavelength-specific single mode optical fiber with a diameter of 50 μm. The incident laser beam is collimated *via* an achromatic lens and passes a holographic band pass filter (to remove the Raman spectrum of the quartz fiber), before it is focused onto the sample through the microscope objective. A Nikon Fluor (60x/1.00 NA) water immersion or a Nikon Plan (100x / 0.90 NA) objective was used in the studies reported.

Raman backscattered radiation is collected through the same microscope objective, and passes a holographic edge filter to block Rayleigh scattering and reflected laser light, before being focused into a multimode optical fiber. The single mode input fiber and the multimode output fiber provide the optical apertures for the confocal measurement. The light emerging from the output optical fiber is dispersed by a 30 cm focal length, f/4 Czerny-Turner monochromator, incorporating a turret with 3 interchangeable gratings (1800/mm, blazed at 500 nm, 600/mm, blazed at 500 nm and 600/mm, blazed at 750 nm). The light is finally detected by a back illuminated deep-depletion, 1024 x 128 pixel CCD camera operating at – 82 ^{o}C.

The sample is located on a piezo-electrically driven microscope scan stage with X-Y resolution of ca. 3 nm and a repeatability of ± 5 nm, and Z resolution of ca. 0.3 nm and ± 2 nm repeatability. The lateral and axial spatial resolution, δ_{lat} and δ_{ax}, are determined by the diffraction limit, as discussed before:

$$\delta_{lat} = 0.61\ \lambda / NA \qquad \delta_{ax} = 2\ \lambda\ n / (NA)^2 \qquad (3)$$

where λ is the wavelength of exciting light, n the refractive index, and NA the numeric aperture of the objective.

The spectral resolution depends on the excitation wavelength and grating groove density; furthermore, the spectral resolution varies significantly over the spectral range projected onto the CCD detector. For 488 nm excitation and the 600/mm grating, the optical resolution varies from about 5.5 cm^{-1}/ data at about 200 cm^{-1} to about 3.3 cm^{-1}/ data point at 4500 cm^{-1}. The 1800/mm grating compresses the wavenumber coverage to about 1400 cm^{-1}. Spectral data hypercubes, consisting of the individual spectra, along with the voxel coordinates where each spectrum was collected, were produced by raster-scanning the sample through the focal point of the Raman microscope. These data sets contain between 100 x 100 and 150 x 150 spectra, collected at a spatial step size of between 300 and 500 nm, and dwell times of 0.2 to 0.5 sec / data point, and required a total acquisition time between 50 minutes to 3 hours.

2.3 Image Processing

The differences in spectral features of individual Raman spectra from different regions of a eukaryotic cell are quite small, and generally at or below the noise superimposed on the Raman spectra. Thus, simple spectral inspections, or univariate methods of analysis of Raman hyperspectral data sets reveal only a fraction of the information contained within the spectral data. We found multivariate methods of analysis to be much more powerful in extracting small, yet relevant variations in the spectra collected from different regions of a eukaryotic cell, and for the construction of pseudo-color images from these datasets.

In this section, we introduce two methods of multivariate data analysis used in this research. The two methods are quite different, and were used to visualize different aspects in a data set. One of these methods, Hierarchical Cluster Analysis (HCA), is an unsupervised method that clusters data by their similarity. To this end, spectral distances are calculated and spectra are assigned to clusters based on these distances. Vertex Component Analysis (VCA), and the other hand, is a method that decomposes a dataset into "component" spectra that are most dissimilar. Both methods have distinct advantages and disadvantages, and may be used to determine different features in a dataset.

Since multivariate methods may be susceptible to artifacts contained in the data, all raw spectra in the data cubes were pre-processed to remove cosmic ray artifacts, and to eliminate spectra devoid of any signal. The resulting pre-processed data sets were subsequently analyzed by HCA and/or VCA to yield the pseudo-color images shown in subsequent figures.

Hierarchical Cluster Analysis

HCA is a powerful method for data segmentation based on local decision criteria. These criteria are based on finding the smallest "distances" between spectra, where the term "distances" may imply Euclidean or Mahalanobis distances, or correlation coefficients[6]. In the latter case, HCA starts by computation of the spectral correlation matrix, **C** according to

$$\mathbf{C} = \mathbf{S}^{\mathbf{T}}\,\mathbf{S} \qquad (4)$$

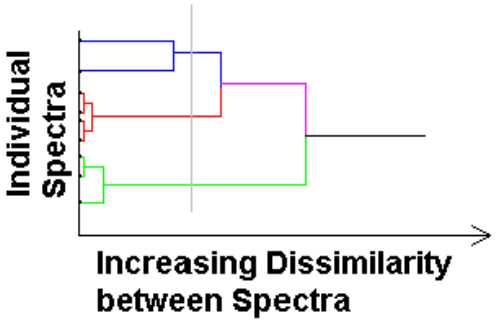

Figure 2. Schematic of Clustering Process. Individual spectra are shown as points along the Y-axis. The merging of spectra (or clusters) is indicated by a vertical line, placed at the level of dissimilarity at which merging occurred.

where each spectral vector $S(\nu_N)$ consists of N equidistant intensity points. The **C** matrix is a $(n \cdot n)$ matrix where n is the number of spectra in the data set. In this matrix, the off-diagonal terms C_{ij} are the correlation coefficients between spectra i and j.

The correlation matrix is subsequently searched for the two most similar spectra, *i.e.*, two spectra k and l for which the correlation coefficient C_{kl} is closest to unity. Subsequently, these two spectra are merged into a new object, or cluster, and the correlation coefficient of this new object and all other spectra is recalculated. In this process, the dimensionality of the correlation matrix is reduced by one. The process of merging is repeated, but the items to be merged may be spectra, or clusters. In the merging process, a membership list is kept that accounts for all individual spectra that are eventually merged into a cluster. This may be visualized by a dendrogram, which indicates at what level of dissimilarity any two spectra or

objects were merged. We have used Ward's algorithm [7] for the process of merging of spectra, and the repeated calculating of the correlation matrix. Once all spectra are merged into a few clusters, color codes are assigned to each cluster, and the coordinates from which a spectrum was collected is indicated in this color. In this way, pseudo-color maps are obtained that are based strictly on spectral similarities. Mean cluster spectra may be calculated that represent the chemical composition of all spectra in a cluster.

HCA assigns cluster membership on a yes/no basis: a spectrum is either a member of a cluster, or it is not. This assignment is based strictly on similarity, and requires no fitting to any reference spectra. We found that HCA reproduces anatomical – architectural features of cells and tissues exceedingly well, even if the spectral differences are too small to be perceived by eye. The resulting "mean cluster spectra", obtained by averaging all spectral patterns in a cluster, often exhibit sufficiently high spectral quality to allow assignment of small chemical or biochemical variations in sample composition over a cell or tissue map.

The disadvantage of HCA is that the correlation matrix is of dimension n^2; thus, if a 100 x 100 point map is collected, **C** is of dimension 10,000 x 10,000. Thus, the memory requirements, and the time necessary for searching this 10,000-dimensional space, are enormous. Typical execution times for a 100 x 100 pixel map are about 2 hours, using fast 64 bit processors running under Windows XP64, and 8 Gbyte of RAM.

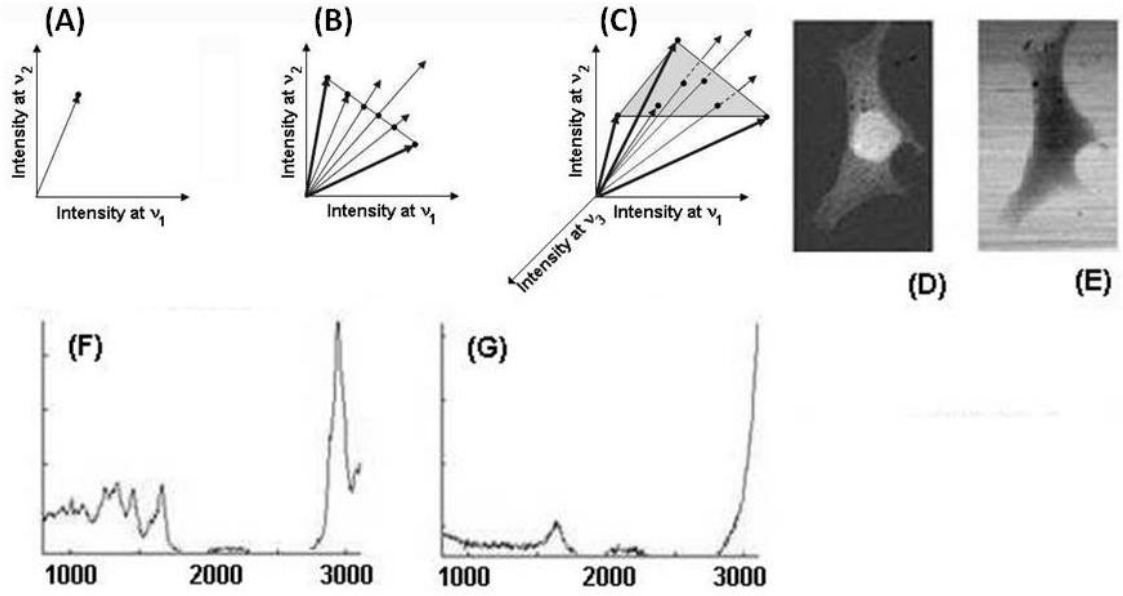

Figure 3. (A,B) Representation of spectral data sets observed at 2 color points and (C) at 3 color points. (D) and (E): Abundance maps for endmember 1 (Panel F) and endmember 2 (Panel G) obtained *via* VCA of a cell. In panels (D) and (E), brighter hues indicate larger contributions of a given endmember.

Vertex Component Analysis (VCA)

VCA uses a completely different approach to reduce the dimensionality of data. Each spectrum is represented as a vector in N-dimensional space, where N, as defined before, is the number of color elements in each vector. This representation may not be too obvious to spectroscopists; thus, it will be elaborated upon in some detail. Imagine that a spectrum is recorded at two frequencies (or channels) ν_1 and ν_2 only. Then, each spectrum can be represented by a vector shown in Figure 3A which indicates the intensity contributions along channels ν_1

and ν_2 to the spectral vector. If two spectra are identical, they will have two identical vectors; two spectra having the same "composition" but different total intensities will have parallel vectors of different length. Figure 3B shows different spectra in two-channel space; their vectors pass through a line as indicated.

For spectra composed of three channels or frequencies, a quiver of vectors is obtained whose endpoints pass through a triangle, as shown in Figure3C. For spectra observed at four colors, the endpoints of the vectors pass through a tetrahedron. In general, the progression from point to line to triangle to tetrahedron *etc.* is known in geometry as a simplex. A simplex describes a p – dimensional hull, or polytop, that possesses p+1 corners.

The principle behind VCA is the assumption that the most extreme vectors in the original representation are "pure component spectra", or endmembers. These endmembers are indicated in Figure 3C as the vectors passing through the corners of the shaded triangle. VCA proceeds from the original dimensionality (in our case $N \approx 1000$, the number of color points in each Raman spectrum) and reduces the dimensionality step-by-step in a process known as 'orthogonal subspace projection'. In each of these steps, the problem is reduced from a p-simplex to a $(p-1)$-simplex while maintaining the relative orientation of the spectral vectors. The process is terminated when the number of endmembers reaches a pre-determined level. Finally, all spectral vectors S in the data set are expressed as linear combinations (linear mixtures) of the pure component (endmember) spectra M according to

$$S = M\alpha + n \qquad (5)$$

where α is the contribution of each endmember to a spectrum and n is residual noise. This abundance, or expansion coefficient, is in the range $0 < \alpha < 1$. Plotting the α-values of one endmember for all spectra in a data set yields an abundance map, shown in Figure 3D and 3E. For example, Figure 3E shows the abundance map for the water endmember; the corresponding water endmember is shown in Figure 3G. Similarly, Figure 3D shows the abundance map for a protein/nucleic acid endmember, shown in 3F. In order to depict the contributions of more than one endmember in an image, individual endmember maps are converted to RCB code and overlaid.

The "spectral unmixing" described so far does not necessarily find the true spectral bases sets. Rather, the outliers in the quiver of vectors are considered the endmembers. In a map of a human cell, for example, VCA will not necessarily produce a pure spectrum of DNA, since no pixel in the sample is due to pure DNA (DNA is always associated with histone proteins). Thus, the best one can achieve with VCA is the decomposition of the spectra into a few basis spectra, or endmembers, which represent the degree to which spectra can be unmixed. We found that for cells contained in aqueous environment, one endmember spectrum is always that of pure water (which is truly an endmember). Other endmembers will contain the most significant spectral features of the remainder of the cell: in the examples to be discussed below, the spectral features of water + protein, and the features of phospholipids, are found prominently in the endmember spectra.

3. Results

3.1 2-D and 3-D Spectral Images of Individual Cells

As an example of the methodology discussed above, we present in Figure 4 confocal Raman images of a hydrated exfoliated oral mucosa cell. These cells can be harvested from the inside of the cheek of volunteers, and deposited after washing on a CaF_2 or fluorescence-free

quartz microscope slide. Figure 4A shows a bright-field image of the cell in aqueous media; therefore, the contrast in this image is quite poor. However, one can just detect the nucleus and the cytoplasm, which does not adhere well to the substrate. In fact, some parts of the cytoplasm are above a thin layer of water that is in contact with the substrate. Figure 4B is a pseudo-color map of the cell constructed, *via* HCA, form 14,400 individual spectra collected using a 60x water immersion objective (NA = 1), and about 15 mW laser power at a wavelength of 514.5 nm. The theoretical pixel size corresponding to these experimental conditions is about 320 nm laterally; however, spectra were collected at a 500 nm grid (*i.e.*, the image was undersampled slightly). The depicted area measures 60 μm x 60 μm (120 x 120 pixels at 500 nm/pixel).

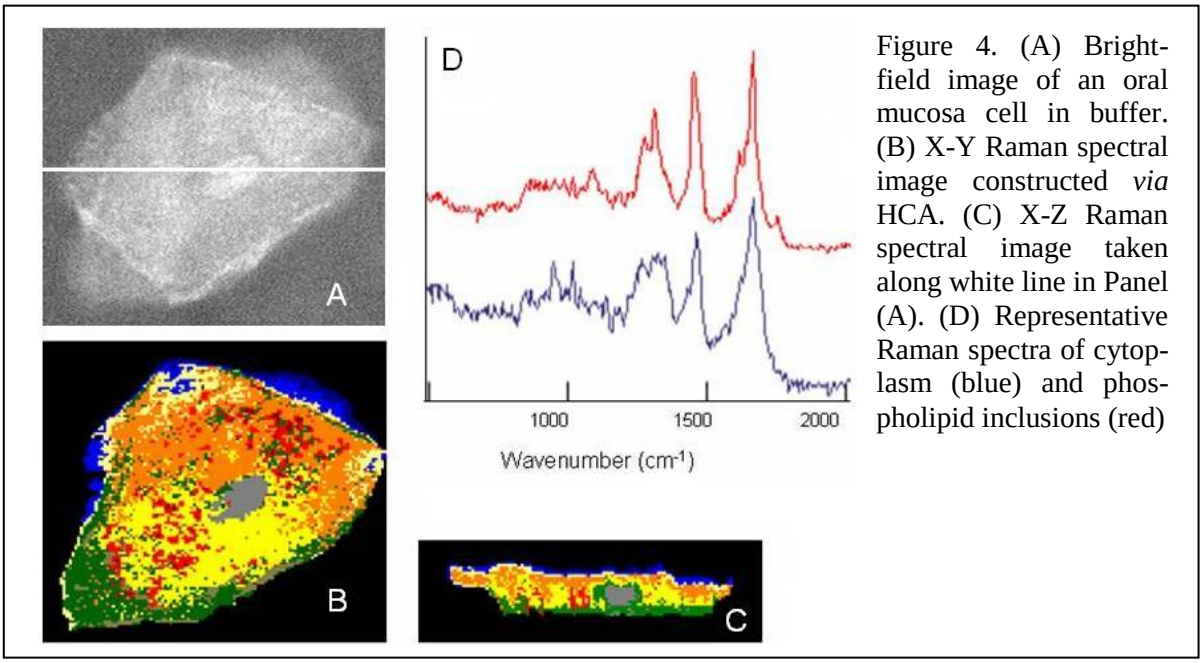

Figure 4. (A) Bright-field image of an oral mucosa cell in buffer. (B) X-Y Raman spectral image constructed *via* HCA. (C) X-Z Raman spectral image taken along white line in Panel (A). (D) Representative Raman spectra of cytoplasm (blue) and phospholipid inclusions (red)

Whereas the image shown in Figure 4B was constructed by scanning the microscope stage in a raster pattern in the X – Y plane, Figure 4C shows an X-Z section of the cell. Here, we use the fact that the measurement is carried out truly confocally, and the laser beam can be focused well below the surface of the cell. By moving the sample in a raster pattern in the X – Z plane, we can construct an optical image from the surface of the cell down to the substrate. The scan shown in Figure 4C was taken along the white line in Figure 4A. The X-Z scan demonstrates that parts of the cytoplasm are not in contact with the substrate.

The images in Figures 4B and C demonstrate the excellent image quality and biochemical information that is available from Raman spectral imaging, followed by multivariate data analysis, which readily distinguishes the nucleus (gray) from the cytoplasm, shown in blue, green, yellow, orange and red colors [8]. The green and blue regions are from areas that do not adhere well to the substrate, and contain larger water spectral contributions. Figure 4D shows mean cluster spectra from regions of the cytoplasm: the red trace in Figure 4D corresponds to the red spots in Figure 4B, which differ in chemical composition from the surrounding cytoplasm (blue trace in Figure 4D). The latter spectrum is typical for high protein contributions, whereas the former contains phospholipid features. This image demonstrates the heterogeneity of components in the cytoplasm, and shows nicely the details on the morphology of a stratified, mature squamous cell.

Figure 5 shows a comparison of HCA and VCA results of another cell type, oocytes (egg cells). These cells assume very different morphology, as they are nearly spherical in shape,

and even larger than the epithelial cell shown in Figure 4. The oocyte shown here, derived from mice, is devoid of a nucleus, but shows large heterogeneity in chemical composition in the cell. The maturity of the oocyte can be determined by monitoring the heterogeneity of the composition of the cell; knowledge of the maturity, in turn, influences the success of *in-vitro* fertilization. The discussion of the biochemical aspects is beyond the scope of this chapter. Here, we wish to show how Raman spectral imaging can help establish the processes of cell maturation [9].

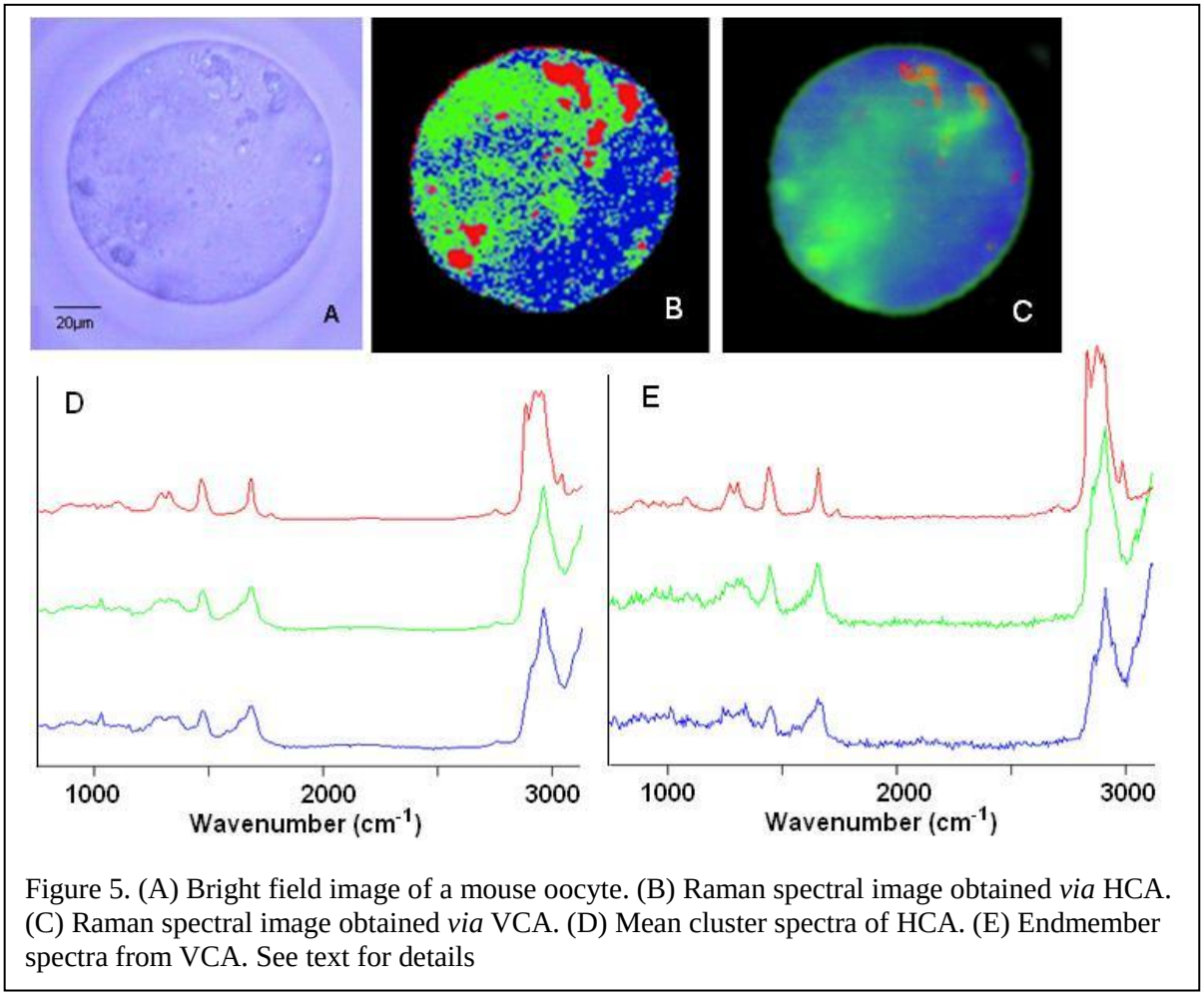

Figure 5. (A) Bright field image of a mouse oocyte. (B) Raman spectral image obtained *via* HCA. (C) Raman spectral image obtained *via* VCA. (D) Mean cluster spectra of HCA. (E) Endmember spectra from VCA. See text for details

The data set collected for the oocyte is from an X – Y plane near the equator of the cell, which measures about 100 μm in diameter and thus, represents a confocal section of the cell. In this plane, data analysis *via* HCA detects significant variance in cell composition, as shown in Figure 5B. The mean cluster spectra corresponding to the red, green and blue areas in 5B are shown (using the same color code) in Figure 5D. Since the spectral traces represent mean cluster spectra of many thousands of spectra, the signal quality is quite good, and one can immediately discern the spectral differences between the red trace (which represents the spectrum of nearly pure phospholipids) and the blue and green traces, which represent mostly protein features. We attempted to utilize specific stains for particular cellular components, and re-image the cell, in order to correlate the Raman images with other imaging modalities. These experiments failed for oocytes since these cells are nearly spherical and so thick that it is impossible to image the same focal plane twice in a row, which is possible for thinner cells. However, we were able to correlate Raman and fluorescence images for thin, adherent cells and assign specific components of the Raman images. This is described later in this section.

The image resulting from VCA is shown in Figure 5C, and the corresponding endmember spectra are displayed in Figure 5E. These spectra have significantly lower signal quality, since they represent the spectra from one single voxel, whereas the mean cluster spectra displayed in 5D are average spectra. Nevertheless, there is good agreement between the mean cluster and the endmember spectra, indicating that both methods pick up similarly relevant spectral features. The VCA map appears a little more diffuse than the HCA map. This can be understood from the fact that HCA assigns a spectrum to a cluster according to a yes/no decision branch; *i.e.*, a spectrum is in one cluster and not the others. VCA, on the other hand, will assign the voxels by a percentage of endmember contribution, and a voxel spectrum could be represented by a 50:50 split between endmembers. Thus, one expects certain differences between the images obtained *via* the two methods. One also could interpret the differences in view of the fact that VCA determines endmembers that are the most dissimilar, whereas HCA places spectra that are most similar into one cluster.

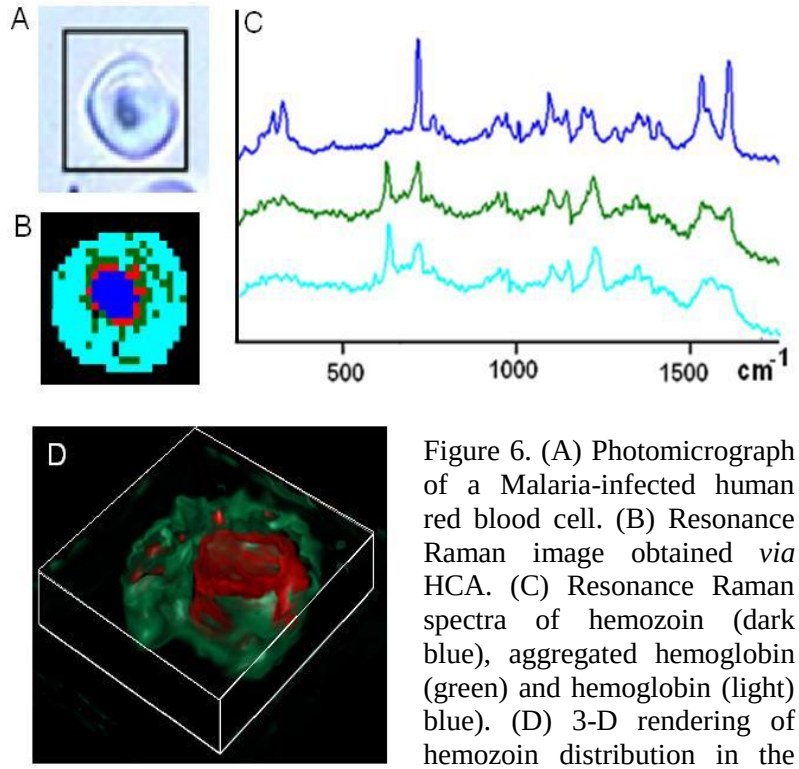

Figure 6. (A) Photomicrograph of a Malaria-infected human red blood cell. (B) Resonance Raman image obtained *via* HCA. (C) Resonance Raman spectra of hemozoin (dark blue), aggregated hemoglobin (green) and hemoglobin (light) blue). (D) 3-D rendering of hemozoin distribution in the cell

We now turn to the discussion of 3-D Raman images of human red blood cells (erythrocytes). To our knowledge, this is the first 3-dimensional image reconstruction of a Raman spectral image of an entire human cell. In particular, we were interested in imaging the effect of malaria infection on red blood cells. The malaria parasite digests the hemoglobin in the red blood cells, but is left with the heme group, which is toxic to it. Thus, the parasite deposits the heme into a semicrystalline, insoluble form known as hemozoin. The studies reported here actually used the resonance Raman Effect to collect the data sets. Resonance Raman spectroscopy (RRS) is a form of Raman spectroscopy where the exciting laser falls within an electronic transition of the sample molecule. It is a widely applied method to study heme proteins, and other strongly colored samples. RRS will be briefly mentioned again in Section 4.

Figure 6A shows a visual microscopic image of a parasite-infected human red blood cell, measuring *ca*. 9 μm in diameter. The dark feature in its center is the hemozoin. A RRS/HCA-derived image of this cell is shown in Figure 6B, with the RRS features of three different regions shown in Figure 6C. Notice that these spectra, excited at 632.8 nm, bear no similarity with protein or other component spectra shown in prior figures, since the RRS spectra of heme proteins only detect the vibrations of the heme chromophore, and not the protein

around the heme. Again, HCA has no difficulty discerning the different spectral features between intact hemoglobin (light blue) and the degraded hemozoin (dark blue).

The cell shown was imaged at 30 x 30 pixels, using 500 nm step size. In addition, 8 different image planes were collected confocally, and the resulting 7200 spectrum data set was analyzed to yield a 3-dimensional representation of the hemozoin distribution in the erythrocyte. This is shown in Figure 6D. It should be re-emphasized that the images in Figure 6B and 6D use the inherent spectral difference between the cellular components, and are truly derived from label-free methods.

The last example of Raman images in this section deals with the label-free visualization of the mitochondrial distribution in cells. Mitochondria are the site of the oxidative phosphorrylation in a cell, and thus, are responsible for a major part of a cell's energy production. Disruption of the biochemical functions of the mitochondria is a major pathway of apoptosis (programmed cell death), and has enormous pharmaceutical and pharmacokinetic applications. The number of mitochondria in a human cell is very large, and they tend to be found in the perinuclear region. Sometimes, mitochondria form tubule-like structures within cells,

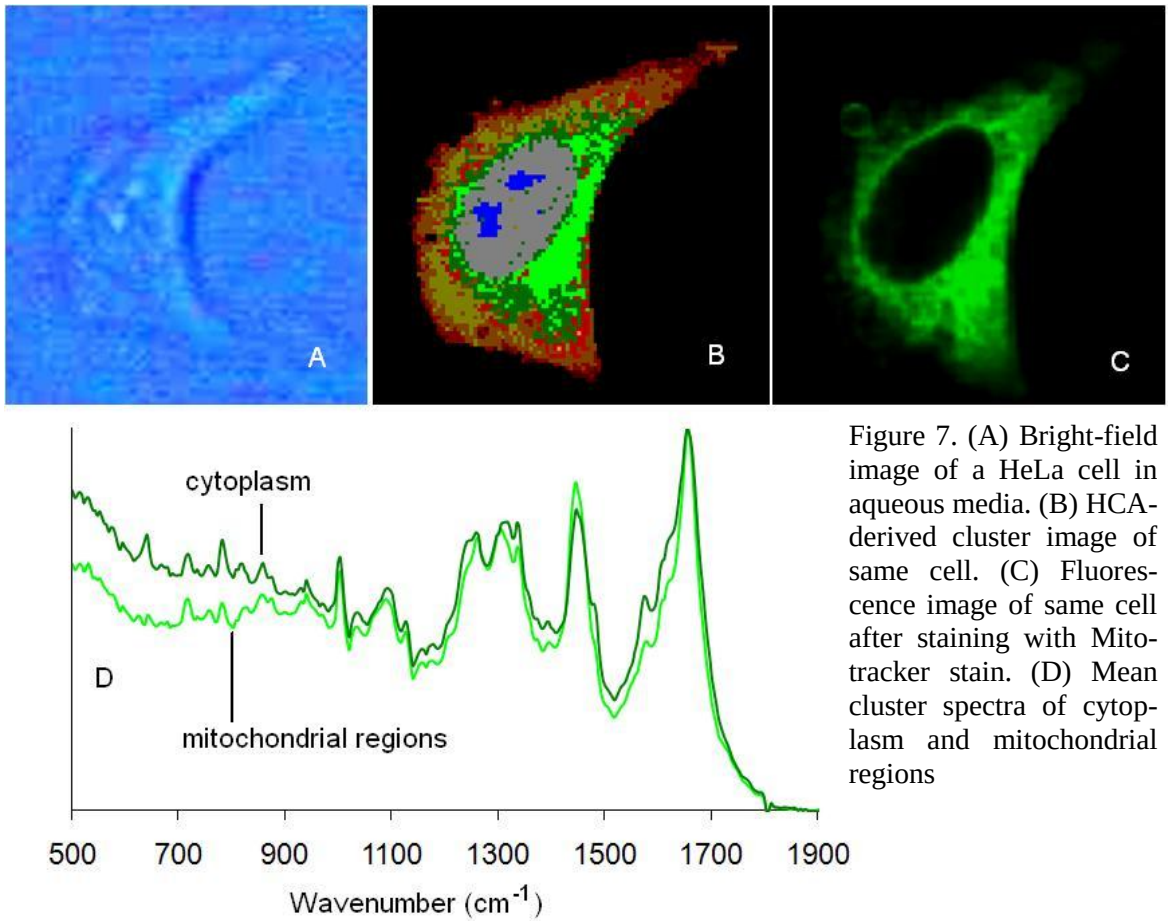

Figure 7. (A) Bright-field image of a HeLa cell in aqueous media. (B) HCA-derived cluster image of same cell. (C) Fluorescence image of same cell after staining with Mitotracker stain. (D) Mean cluster spectra of cytoplasm and mitochondrial regions

which have been detected by fluorescence microscopy. Here, we wish to demonstrate that Raman micro-spectroscopy, coupled to multivariate methods, can detect aggregated mitochondria in the perinuclear region, and mitochondrial tubules.

Figure 7 shows results for an epithelial cervical cancer (HeLa) cell grown onto a CaF_2 substrate using standard cell culture procedures. Cells adhering to the substrates were formalin-fixed, and subsequently immersed in a drop of BSS solution. The cells assume a characteristic shape and size, typically between 40 and 60 μm in the X – Y dimension and about 5 - 10 μm thick. Figure 7A is a bright field image of a cell in aqueous medium, taken through

20x objective. The quality of the bright field image is low, since the aqueous medium, in which the cell is immersed, tends to reduce the visual contrast.

Raman images were collected using a 60x water immersion objective, 488 nm excitation and 500 nm x 500 nm raster step size. Figure 7B shows a Raman map of the cell shown in Figure 7A obtained from HCA of the data set. The Raman image reveals the large nucleus (gray), typical for actively growing cells, and the surrounding cytoplasm (green, red and brown hues). The nucleus contains distinct nucleoli (blue). The distinction between nucleus and nucleoli is particularly gratifying, since their chemical composition is quite similar: the nucleus consists mostly of nuclear proteins and DNA, whereas the nuclei consist mostly of protein and RNA. Immediately after Raman data acquisition, a fluorescent stain specific for mitochondria (Mitotracker Green® FM, Invitrogen, Carlsbad, CA) was added to the sample without disturbing the optical settings of the instrument, which makes registration of the resulting images possible. Fluorescence images were collected *ca.* 20 min. after the stain was added, using the confocal Raman instrument described above and 488 nm excitation. Figure 7C shows the fluorescence image indicating the mitochondrial distribution of the cell. Bright green areas correspond to highest fluorescence intensity and mitochondria concentration, which occurs in the perinuclear region. A comparison of Figures 7B and 7C reveals that the regions, from which significant fluorescence due to the Mitotracker® stain is observed, co-localizes very well with the Raman cluster shown in dark and bright green in Figure 7B. Thus, we conclude that these green clusters are due to cytoplasm of the cell containing larger numbers of mitochondria.

Since HCA can distinguish the mitochondria-free and mitochondria-rich areas of the cytoplasm, it is interesting to compare the mean cluster spectra from these two regions. We found that the mean cluster spectra obtained for cytoplasmic and mitochondrial regions shown in Figure 7D are quite similar, yet show subtle differences that could be reproduced for several cells studied [10]. The number of spectra contributing to these mean cluster spectra is on the order of several hundred; consequently, the observed signal-to-noise ratio for the mean cluster spectra, and the spectral reproducibility, are quite good. All mean cluster spectra, (even those of the nucleus and the nucleolus, not shown) are dominated by protein bands (the amide I vibration at 1655 cm^{-1}, the extended amide III region between 1270 to 1350 cm^{-1}, and the sharp phenylalanine ring stretching vibration at 1002 cm^{-1}). This is not surprising, given that the major component in all regions of the cell is protein. The spectral differences between the nucleus (composed predominantly of protein and DNA) and the nucleoli (composed mainly of protein, DNA and ribosomal RNA) are expected to be small; yet, HCA can distinguish these regions inside a cell quite readily. However, the spectral intensity patterns for the mitochondria and the remainder of the cytoplasm are quite similar in peak positions, although relative intensities do vary. These intensity shifts, however, cannot be interpreted at this time in a meaningful way. We had hoped to detect the resonance Raman patterns of the cytochrome species in the mitochondria, using different excitation wavelengths, but were not able to do so using the laser colors available in our Raman microscope.

Although the spectral images reported in this paper were collected using the 488 nm line of an Argon ion laser, we observed no fluorescent interference in the Raman spectra of the unstained cell. At this point, it is not clear why there was no fluorescence for the HeLa cells reported here, since the conventional wisdom is that visible excitation cannot be used for work on cells and tissue. For cultured cells, we mostly observed fluorescence-free spectra for both fixed and unfixed cells, both in aqueous medium and as dried cells. We have observed fluorescence in a few other cell types, usually originating from very small regions within the cells that may be contaminations. In the absence of fluorescence, the 488 nm Argon ion line offers enormous advantages over red or near IR laser excitation wavelengths, at for example

633 or 785 nm. These include a higher scattering cross section (by about a factor of 6), significantly higher detector sensitivity, and better spatial resolution due to the shorter wavelength.

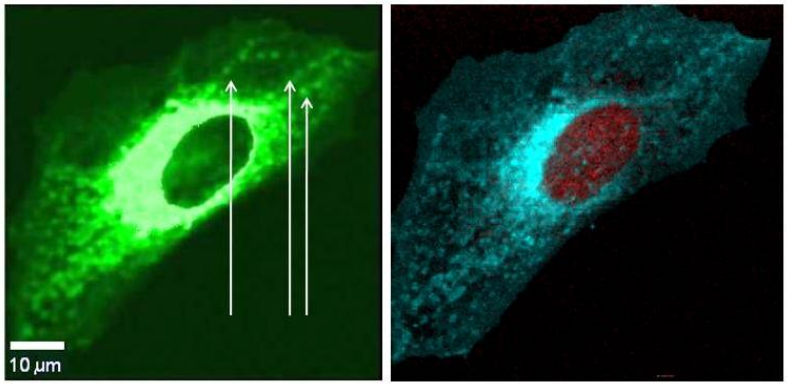

Figure 8: Detection of mitochondrial tubules by (A) fluorescence imaging, and (B) Raman microspectroscopy / VCA. The raster step size was 250 nm.

To demonstrate the sensitivity of Raman spectral imaging toward detecting small, distinct structures inside cells, we present results showing that the tubular structures that may be formed by mitochondria can be detected. Figure 8A shows the fluorescence image, after staining with Mitotracker Green® FM stain, of a HeLa cell. The corresponding Raman spectral image, constructed *via* VCA, is shown in Figure 8B. The data set responsible for this image was collected at a raster step size of 250 nm, with 488 nm excitation. Since the theoretical lateral spatial resolution (290 nm) is approximately the same as the step size, detection of objects about 290 nm in size should be possible. In practice, the smallest of the light blue features in Figure 8B are somewhat larger, about 2 – 3 pixels. These features co-localize very well with the microtubules seen in the fluorescence image shown in Figure 8A (at the end of the white lines pointing at them). These results confirm that Raman spectral imaging is a novel, label-free imaging methodology for biological systems.

3.2 Slow dynamic Processes in Cells: uptake of drugs and drug delivery systems

Since Raman imaging can be carried out on unstained cells, it is a powerful tool for following dynamic processes in live cells, or cells fixed at certain time points during a dynamic process. Since data acquisition at this point in time is still very slow, slow dynamic processes, such as the uptake of drugs or drug delivery particles that take a few hours are ideal candidates for cellular dynamics studies. In the past, such processes have been studies *via* fluorescence microscopy; however, as pointed out before, the actual fluorescent label needed to observe the desired uptake may influence the uptake processes and equilibria.

Apart from imaging subcellular features, as discussed in the previous section, Raman imaging may provide an opportunity to follow the uptake of molecules into cells. We have reported the detection of specific drugs that diffused into molecules *via* passive transport [11]. In order to facilitate the detection of these drugs, they were modified to incorporate, or naturally contained, certain groups that exhibit strong signals in regions where the Raman spectrum is devoid of other signals. Although these initial studies were successful, the drug concentration achievable inside a cell by diffusion was so low that the drugs just barely could be detected. We report here the next generation of drug uptake studies, which are based on the use of deuterated drugs or carrier systems. One way to distinguish molecules incorporated inside cells from those naturally occurring inside it is to use deuterated compounds [1]. Deuterium labeling of either the drug or the drug delivery system is a powerful method since the C-D stretching vibrations are shifted away from those of C-H groups by a factor of square root of the ratio of masses of D and H, or about a factor of 1.4. Thus, C-D stretching vibrations occur around 2150 cm^{-1}, in a region devoid of any signals in the Raman spectra of cells

and cellular components. The deuterium "label" is invisible to the cell, since the isotopic species occupies nearly exactly the same volume, and acts chemically nearly identically to hydrogen atoms.

We report here results from three different studies ongoing in our laboratory: the uptake of deuterated liposome particles into cells, the uptake of drug-loaded micelles into cells, and the uptake of solid nanoparticles loaded with drugs into cells. In some of these systems, the drug carrier systems exhibited spectral features sufficiently different from cellular features that the drug carriers could be visualized without deuteration.

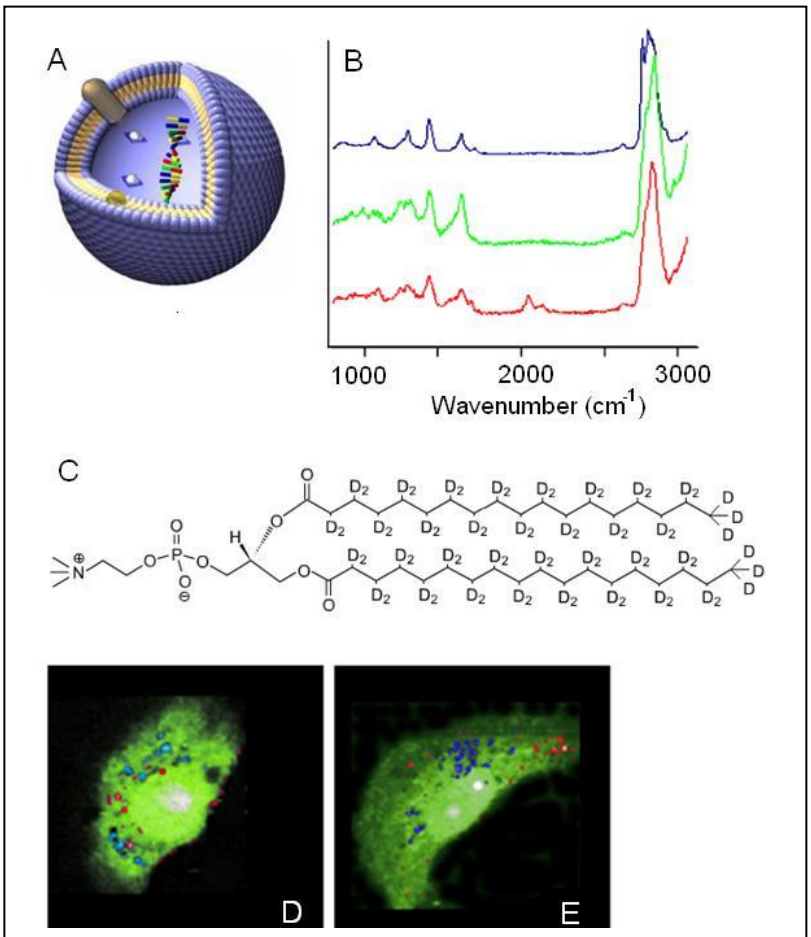

Figure 9: (A) Schematic of lipid bilayer liposome, shown with a drug load. (B) Endmember spectrum of naturally occurring phospholipid inclusions (blue), protein (green) and deuterated phospholipids (red) (C) structure of DSPC-d_{70}. (D) and (E): Raman spectral images of two cells after incubation with DSPC-d_{70} liposomes. The red dots are due to the deuterated liposome particles.

We begin this discussion by demonstrating the cellular uptake and intracellular fate of lipid-based nanoparticles known as liposomes (Figure 9A). These are bilayer-based nano-spheres with sizes ranging from about 50 to 300 nm. Currently, liposomes are used for drug delivery purposes, including intracellular drug and gene delivery [12, 13]. Many aspects related to the detailed mechanisms of the liposome - cell interaction, including the exact uptake mechanism and the ultimate fate of the liposomes, remain unresolved.

Deuterated liposomes were prepared according to literature procedures [14] from a dried lipid film cast from a chloroform solution of DSPC-d_{70} (Figure 9C; Avanti Polar Lipids, Inc., Alabaster, AL). This film was hydrated and vortexed with HEPES-buffered saline (HBS), pH 7.4, at a DSPC concentration of 1.6 mM to form liposomes. The resulting liposomes were sized through double stacked 200 nm pore size polycarbonate membranes (Nucleopore), and their size was determined by a Submicron Particle Size Analyzer (Coulter Electronics). Human breast adenocarcinoma MCF-7 cells were incubated for different time intervals with deuterated liposomes at lipid concentration of 2 mg/mL. After incubation, the cells where fixed in a formalin-phosphate-buffered solution and subsequently washed and submerged in phosphate-buffered saline, to maintain the shape of the cells in their aqueous environment.

Figure 9D and E show Raman images, reconstructed *via* VCA, of MCF-7 cells incubated with deuterated liposomes for 12 hours at a concentration of 2 mg/mL. In each cell, the nucleus (bright green) with nucleoli (white) can be discerned easily. The nuclei are surrounded by the cytoplasm exhibiting a number of blue and red spots. The blue spots are due to phospholipid inclusions that occur naturally in these breast cancer cells. The blue trace in Figure 9B is from these naturally occurring inclusions. The green spectrum in Figure 9B represents a spectrum from within the cytoplasm, and reflects its protein composition. The red trace in Figure 9B is due to the deuterated liposomes and protein, as indicated by the clearly visible set of peaks around 2150 cm^{-1} due to the C-D stretching vibrations. Therefore, the red areas in Figures 9D and 9E, can be assigned to deuterated liposomes, or aggregates of them. To ascertain that the observed deuterated liposomes are within the cytoplasm, and not just adsorbed on the cell surface, a depth profile (X – Z scan) was collected as well (results not shown). The scan demonstrated clearly that the deuterated liposomes penetrate throughout the cell body, which is about 10 μm thick, which was found to be typical for MCF-7 cells.

The uptake of liposomes could be accelerated significantly by modification of the liposomal nano-carriers by cell-penetrating peptides, such as the HIV-1 *trans*-activating transcriptional activator-derived TAT peptide[14]. These carrier systems are currently considered a very promising way to bring various drugs, including protein and peptides, into cells. Here we demonstrate the feasibility of Raman imaging to follow the uptake of TAT peptide-modified deuterated liposomes (TATp-liposomes). TATp-liposomes were prepared by adding TATp-PEG_{2000}-PE (pegylated phosphatidyl ethanolamine) to the lipid film, which incorporates into the liposome membrane structure. Liposomes were subsequently sized as described above. Purified TATp was received from Tufts University Core Facility (Boston, MA).

The most important result of this study was that the uptake is enormously accelerated by TATp, confirming previous experiments [15]. This uptake was clearly seen already after 3 hours for TATp-liposomes and only after 12 hours for plain liposomes. Although very small deuterated regions can be detected early in an uptake experiment, aggregation or incorporation of the deuterated phospholipids into other membrane structures occurs, resulting in contiguous regions of high deuterium content. The spectral appearances of the C-D stretching region did not change significantly upon uptake in terms of band shapes and peak positions, indicating that the lipid side chains did not undergo substantial conformational changes. However, a reversal of the C-D/C-H ratios for structures around the nucleus implies a wide distribution of DSPC-d_{70}; possibly due to exchange between incorporated phospholipids and phospholipids of intracellular membrane structures over time. We believe that Raman microspectroscopy can be successfully applied to study the interactions of various pharmaceutical nanocarriers, including lipid-based nanocarriers, such as liposomes, within cells. Furthermore, the information from Raman spectral imaging experiments will allow for the optimization of the properties of such nanocarriers in a controlled fashion. In addition, any organic molecule that may be a potential candidate for these delivery systems may be labeled with deuterium, which will allow the fate of the cytologically active compounds to be monitored.

To demonstrate this point, we present in Figure 10 results of the release of a drug from nanoparticles that were loaded with a deuterated drug analogue that can be detected readily by Raman imaging. To this end, nanoparticles composed of poly-ε-caprolactone (PCL), about 150 nm in size, were loaded (20% by mass) with a deuterated, pro-apoptotic drug, N-palmitoyl-(d_{31})-D-*erythro*-sphingosine, a member of the ceramide family whose structure is shown in Figure 10B. We shall henceforth refer to this compound as ceramide-d_{31}. In Figure 10A, we show the Raman spectra of pure PCL, (trace b), pure ceramide-d_{31} (trace a) and of the ceramide-d_{31}-loaded nanoparticle (trace c). In trace C, spectral features of both PCL and ceramide-d_{31} can be readily detected, and the signal intensity ratio of the C-D stretching

bands of the ceramide and the band at ca. 1500 cm^{-1} of the PCL, can be used as a qualitative indicator of whether the loaded drug particle stays intact, or dissolves and releases the drug.

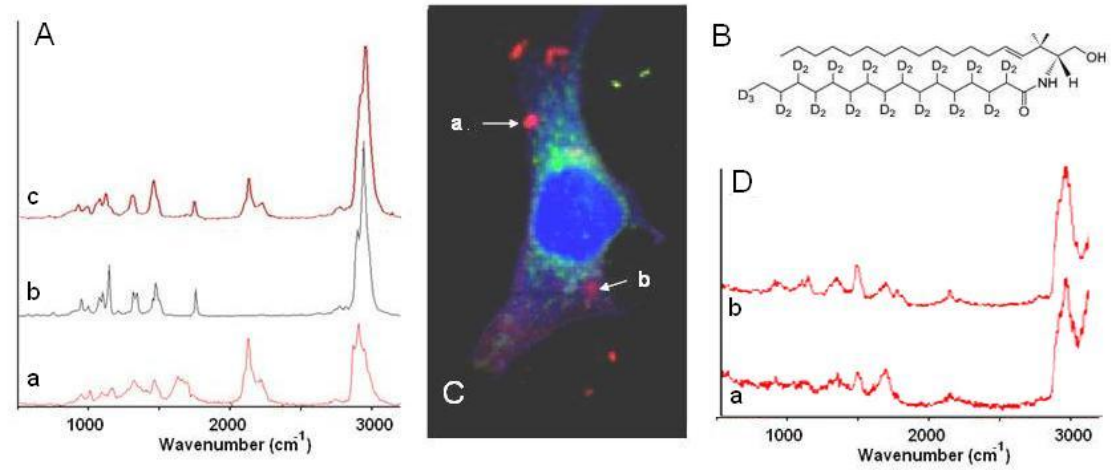

Figure 10. Uptake of drug-loaded nanoparticles into a HeLa cell. Panel (A): Raman spectra of the pure ceramide-d_{31} (trace a), pure PCL, (trace b), and the ceramide-d_{31}-loaded nanoparticle (trace c). Panel (B): Structure of N-palmitoyl-(d_{31})-D-*erythro*-sphingosine (ceramide-d_{31}). Panel (C): Raman spectral image of a HeLa cell incubated for 7 hours with drug-loaded PCL nanoparticles. Panel (D): Raman spectra of points marked (a) and (b) in Panel 10C.

Figure 10C shows a Raman spectral map, constructed *via* VCA, of a cell incubated for 7 hours with the drug-loaded PLC nanoparticles. This image clearly shows the nucleus in bright blue color, the perinuclear regions rich in lipids (either due to mitochondria or endoplasmic reticulum) in green, and bright red spots (*e.g.*, the spot marked "a") due to the presence of C-D stretching signals of the nanoparticles. However, at the spot marked "b", and in several other spots collected from other cells, the ratio of the 1500 cm^{-1} marker band for PCL and the C-D marker bands for the drug changes, indicating that at these spots the degradation of the nanoparticle has released the drug into the cytoplasm. Similar experiments had been attempted using fluorescent labels that were incorporated in the nanoparticles. However, it appears that even in solution outside the cell, fluorescent label molecules were released, and a clear visualization of the drug release inside the cell could not be realized. Raman spectral imaging, on the other hand, offers the advantage of allowing the drug and the nanoparticles to be visualized without the use of an external label. Thus, spectral imaging which utilizes an inherent (or at least chemically indistinguishable) label such as deuterium-substituted side chains offers less perturbing methodology.

4. Future directions: RRS, CARS and SRS imaging

The collection of cellular images, as shown in Section 3 *via* spontaneous Raman scattering is a very time-consuming process, since acquisition of a useable voxel spectrum takes on the order of 200 – 500 msec. Thus, it may take up to a few hours of collection time to assemble a hyperspectral data cube suitable for analysis *via* multivariate methods. The obvious choices to reduce data acquisition time are to produce more scattered photons, and to optimize the optical train to collect and process photons. In commercial Raman microscopes, the efficiency of photon collection and processing has been optimized to such a level that no major gains can be foreseen. In terms of producing more scattered photons, one either can increase the laser power incident on the sample, or use Raman processes with larger scattering cross sections. Laser power, unfortunately, cannot be increased significantly, since any in-

crease in laser power leads to a rapid destruction of the sample due to local heating. This aspect can be understood simply be considering the incident laser power density. Using the instrumentation described in Section 2, we presently illuminate the sample with *ca.* 10 mW of laser power, focused into a spot with a radius of about 200 nm. This amounts to a power density of *ca.* 10^7 W/cm^2, which is about the limit at which a dry, biological sample will be destroyed instantaneously. The use of water immersion objective alleviates the problem somewhat, since the laser power is dissipated more easily into the surrounding volume. We have shown that exposure to these power levels for about one second does not destroy the sample noticeably in an aqueous environment; yet, we have found that the power cannot be increased by more than a factor of 2 or 3 before destruction of the sample occurs, even in aqueous environments. Thus, increasing the laser power is not a valid option.

However, there are several methods to enhance the inherently weak Raman scattering intensities. One of the best-known of these methods is the use of resonance enhancement alluded to in Section 3.1, which may occur if the frequency of the exciting laser approaches the frequency of a real electronic transition. In this case, some terms of the transition polarizability become very large, since the denominator of these terms becomes very small (see eqn. 2 above). The resulting Resonance Raman effect is particularly suitable to enhance certain vibrations of the metal – porphyrin moiety found in heme proteins, cytochromes and a few other proteins. Using resonance enhancement, we were able to image the heme and hemozoin moieties in the erythrocyte images shown in Figure 6. We also could visualize and regions of high cytochrome-450 in certain cell types that over-express this protein. However, resonance Raman imaging is restricted to cases where a chromophore can be accessed easily, and is not a method of enhancing Raman signals in general.

During the past decade, several groups have reported Raman images created by nonlinear effects. In the discussion presented so far, it was assumed that the Raman scattered intensities obey eqn. 1, namely that the scattered intensities depend linearly on the incident laser intensity. This implies that the induced dipole moment, μ, depends linearly on the incident laser field, **E**:

$$\mu = \alpha \mathbf{E} \qquad (6)$$

where the elements of the polarizability tensor α were defined before in eqn. 2. Equation 6 is a microscopic description of the effect of the oscillating laser field on the molecules of the sample. Similarly, this effect can also be described macroscopically in terms of the polarization, **P**, induced by the electric field *via* the dielectric susceptibility, χ:

$$\mathbf{P} = \chi \mathbf{E} \qquad (7)$$

In non-linear Raman spectroscopy, which can be observed at very high field strengths obtainable by ultrashort laser pulses, one needs to take into account the dependence of the induced dipole moment or the polarization on higher powers of the field strength:

$$\mu = \alpha \mathbf{E} + \beta \mathbf{E}\,\mathbf{E} + \gamma \mathbf{E}\,\mathbf{E}\,\mathbf{E} + \cdots \qquad (8)$$

where β and γ are referred to as the first and second hyperpolarizability tensors. The former gives rise to the hyper-Raman effect, whereas the latter is responsible for a number of nonlinear effects such as Stimulated Raman spectroscopy (SRS), Raman Gain spectroscopy (RGS), Raman induced Kerr effect (RIKE), and Coherent Anti-Stokes Raman scattering (CARS). In terms of the macroscopic dependence of the induced polarization on the field strength, one uses the second and third order susceptibility tensors, $\chi^{(2)}$ and $\chi^{(3)}$, to describe the nonlinear effects.

To date, CARS microscopy has been the most widely applied of these methods to reduce image acquisition time, and CARS spectral images of human cells showing exquisite detail have recently reported [16]. Furthermore, CARS images have been produced at video rates, which allow biological processes with fast dynamics to be studied. These results, for example, show in real time the uptake of drugs into skin [17]. CARS images are generally produced by univariate methods, focusing on distinct marker bands in the CARS spectra. Unfortunately, CARS spectroscopy suffers from the presence of a non-resonant scattering background that tends to distort the bandshapes, and makes spectral interpretation more difficult than for spontaneous Raman spectroscopy.

Just very recently, an imaging methodology based on stimulated Raman scattering (SRS) or femtosecond stimulated Raman scattering (FSRS) was reported [18, 19]. These methods will produce spectra that are nearly identical in spectral shapes to spontaneous Raman spectra, but can be obtained significantly faster and free of a spectral background. Although significantly more complex than spontaneous Raman microscopic instrumentation, the SRS technology probably offers the best opportunity to visualize biochemical processes as fast as fluorescence microspectral imaging, but using inherent chromophores of the biochemical components of a cell.

5. Conclusions

In this chapter, results from Raman spectral imaging of biological systems were presented. In general, the images produced of cells, subcellular organization and dynamic processes occurring in a cell have demonstrated that Raman spectral imaging is a viable technique for cellular biology, and produces images of similar spatial resolution as do confocal fluorescence and two-photon fluorescence imaging. The overwhelming advantage of spontaneous and non-linear Raman techniques is the fact that inherent spectral signatures of all biochemical components inside a cell can be sampled, and no labeling is required for the data acquisition. Since Raman techniques sample the molecular vibrational information of the components, rich spectra with many individual peaks are collected, in contrast to fluorescence imaging, where only few and broad transitions are observed. The inherent spectral information content can be exploited by using multivariate methods of analysis, which are particular sensitive to small changes of a few spectral features in the presence of nearly unchanged overall spectra.

6. References

[1] H.-J. van Manen, Y. M. Kraan, D. Ross and C. Otto, *Proc Natl Acad Sci* **2005**, *102*, 10159-10164.

[2] M. Diem, *Introduction to Modern Vibrational Spectroscopy*, Wiley-Interscience, New York, **1993**, p.

[3] G. Placzek in *Rayleigh Streuung und Raman Effekt (Rayleigh Scattering and the Raman Effect), Vol. Vol. VI., 2* **1934**, p. 209.

[4] C. Otto, Greve, J., *The Internet Journal of Vibrational Spectroscopy* **1998**, *2*.

[5] M. Delhaye and P. Dhamelincourt, *J.Raman Spectrosc.* **1975**, *3*.

[6] M. J. Adams, *Chemometrics in Analytical Spectroscopy*, Royal Society of Chemistry, Cambridge, **2004**, p.

[7] J. H. Ward, *J. Amer. Stat. Assoc.* **1963**, *58*, 236-244.

[8] C. Matthäus, B. Bird, M. Miljković, T. Chernenko, M. J. Romeo and M. Diem in *Infrared and Raman Microscopy in Cell Biology, Vol.* Eds.: J. J. Correia and I. Detrich, H.W.), Elsevier, **2008**, pp. 275-308.

[9] B. R. Wood, T. Chernenko, C. Matthäus, M. Diem, C. Chong, A. Brandli, C. Jene, D. McNaughton, M. J. Tobin, A. Trounson and O. Lacham-Kaplan, *Anal.Chem.* **2008**, *80*, 9065-9072.

[10] C. Matthäus, T. Chernenko, J. A. Newmark, C. M. Warner and M. Diem, *Biophys J* **2007**, *93*, 668-673.

[11] C. Matthaeus in *Raman - Microscopy of Individual Cells and Applications Monitoring Drug Uptake, Vol. PhD* City University of New York, New York, **2006**.

[12] L. Serpe, Guido, M., Canaparo, R., Muntoni, E., Cavalli, R., Panzanelli, P., Della, Pepal, C., Bargoni, A., Mauro, A., Gasco, M. R., Eandi, M., Zara, G.P., *J. Nanosci. Nanotechnol.* **2006**, *6*, 3062-3069.

[13] N. M. Rao, Gopal, V., *Biosci. Rep.* **2006**, *26*, 301-324.

[14] C. Matthäus, A. Kale, T. Chernenko, V. Torchilin and M. Diem, *Molecular Pharmaceutics* **2008**, *5*, 287-293.

[15] J. S. Wadia and S. F. Dowdy, *Adv. Drug Deliv. Rev.* **2005**, *57*, 579-596.

[16] H. Kano, *J. Raman Spectrosc.* **2008**, *39*, 1649-1652.

[17] C. L. Evans, E. O. Potma, M. Puoris'haag, D. Conte, C. P. Lin and X. S. Xie, *Proc Natl Acad Sci* **2005**, *102*, 16807–16812.

[18] C. W. Freudiger, W. Min, B. G. Saar, S. Lu, G. R. Holtom, C. He, J. C. Tsai, J. X. Kang and X. S. Xie, *Science* **2008**, *322*, 1857-1861.

[19] E. Ploetz, S. Laimgruber, S. Berner, W. Zinth and P. Gilch, *Applied Physics B* **2007**, *87*, 389-393.